AIAA JOURNAL
Vol. 45, No. 4, April 2007

Experimental Investigations on Indeterminate-Origin V- and A-Notched Jets

T. H. New*
University of Liverpool, Liverpool, L69 3GH England, United Kingdom
and
H. M. Tsai†
National University of Singapore, Singapore 119260, Republic of Singapore

DOI: 10.2514/1.24591

Experimental studies on aspect ratio of 1.5 indeterminate-origin V- and A-notched nozzles using flow visualization and hot-wire anemometry techniques are reported here. Time-sequenced flow visualization images of forced water jets at Reynolds number of 2000 show that the general vortex dynamics of the two nozzle types are largely similar despite the differences in the peak and trough configurations. In addition to vortex lines emanating from both nozzles which result in streamwise vortex pairs forming along both peak and trough locations, consistent bending of the large-scale ring vortices is also observed at some downstream distances away from both nozzle exits, which suggests some limited form of axis-switching behavior. Velocity measurements for unforced air jets issuing from these nozzle types at Reynolds number of 20,500 show that there exist subtle yet discernible quantitative flow differences depending on whether the peak and trough contours are smooth or sharp. Sharp peaks and smooth troughs result in wider jet widths over smooth peaks and sharp troughs, respectively, although the differences become smaller with increasing downstream distance. Jet-width comparisons also reveal crossover locations and hence distortions to the jet cross sections, which further supports the notion of axis-switching behavior observed during flow visualizations. Two axis-switching locations have been found for each of the two nozzle types with the gross general flow behavior similar to those observed earlier for free elliptic jets.

Nomenclature

D	=	jet diameter
f	=	forcing frequency
H	=	mean nozzle height
Re	=	Reynolds number, UD/ν
r	=	radial distance from nozzle exit center
St	=	Strouhal number, fD/U
U	=	mean jet exit velocity
U_{cl}	=	mean jet centerline velocity
$\bar{u}$	=	mean local jet velocity
u'	=	mean velocity fluctuations
z	=	distance from nozzle mean height
δ_w	=	jet shear layer vorticity thickness
ν	=	kinematic viscosity of water
θ	=	momentum thickness

I. Introduction

JET-MIXING enhancement techniques have been studied extensively over the past years due to their immediate applications in many engineering areas such as fuel-injection systems, chemical-mixing processes, and flow-control systems, just to name a few. Over these years, numerous experimental and numerical studies have been carried out to investigate and understand how jet mixing can be further improved over the typical benchmark circular jet geometry and include efforts ranging from using noncircular jet geometries [1–4], to bifurcating and blooming jets [5,6], to jets with tabs [7–9], to swirling jets [10–12], to indeterminate-origin jets [13–18]. It is widely accepted that production of and interactions between large- and small-scale vortex structures are primarily responsible for the jet-mixing phenomenon. Any techniques seeking to improve jet mixing must address the two requirements, and over the years, both passive and active techniques have been proposed and studied extensively to accomplish either one or both of the requirements. However, despite highly significant improvements made in the area of active enhancement techniques such as swirling jets, fluidic excitations, synthetic jets, and mechanical actuators, which in some cases prove superior to passive techniques, passive techniques remain popular in applications that require high levels of operating robustness at minimal cost, energy, and control constraints.

Indeterminate-origin (IO) jets represent one of the more recent examples of passive jet-mixing enhancements and control techniques that are cost-effective and robust. As the name implies, the physical designs and geometrical configurations of these jets are such that their flow origins cannot be defined conventionally at fixed axial locations along the jet symmetry axes due to axial and circumferential variations or undulations along the nozzle lips. Depending on the exact design, the axial undulations along the nozzle lips may either vary smoothly or possess sharp discontinuities at some locations. Because of the complex nature of the resultant flowfields, investigations and subsequent understandings are typically based on relatively simpler nozzle designs. For instance, IO jets with inclined and stepped nozzle exits have been studied previously in terms of the effects of varying the incline angle and step length on the behavior of the jet shear layers [13,14], and they were observed to drastically redistribute the energy content within the jet shear layers. More complex "crown-shaped" IO jets have also been investigated by varying the number and the heights of the peaks and troughs [15] with observations showing the peaks and troughs led to the distinctive formations of small-scale but highly coherent streamwise vortex pairs. Interactions between these streamwise vortex pairs and the large-scale jet ring vortices were found to result in increased mixing between the IO jets and their surroundings, with the roles of the streamwise vortex pairs in the improved entrainment process clarified in the near-field regions. Furthermore, depending on the exact configuration and number of the peaks and troughs, the

Received 12 April 2006; accepted for publication 27 December 2006.

*Lecturer, Department of Engineering, Brownlow Hill.
†Principal Investigator, Temasek Laboratories. Member AIAA.

impact of the streamwise vortex pairs upon the jet could be altered, which led to significantly different jet cross-sectional shapes.

Subsequent investigations on stepped and sawtooth IO jets under strong forcing conditions also revealed jet bifurcation behavior, which led to significant diversion of the jet path from its original streamwise direction [16]. This resulted from the inclined and destabilized vortex rings caused by the stepped and sawtooth nozzle configurations, which led to the formation of secondary structures with opposite inclinations. Despite the need for energy input for such behavior to manifest, this finding significantly suggests that directional mixing enhancements along specific azimuthal planes is possible. Furthermore, studies have also been carried out on the effects of incline-angle variation on the resultant flowfields in inclined IO jets [17], and it was observed that the pairing of the large-scale jet ring vortices depends critically on the nozzle incline angle. Small incline angles led to successful pairings, whereas large incline angles caused the vortex cores to break down before any successful pairing could occur, which agreed well with observations reported by another study [18] where it was postulated that the breakdown could be attributed to different vortex-stretching rates along the jet shear layer caused by nonaxisymmetric vortex rollup.

Despite good understanding of some localized effects caused by certain IO nozzle designs, knowledge on how the large- and small-scale vortex structures are initiated, interacted with one another, and developed remain largely incomplete. Hence, a flow visualization study [19] was carried out recently in an attempt to reconcile the earlier experimental findings such that a plausible flow model could be constructed for IO jets with V-shaped notches or cuts as part of an overall effort to better understand the implications of various nozzle designs. Interestingly, the rotational senses of the streamwise vortex pairs at both peak and trough locations observed during the course of the study were found to be different from those observed previously [15]. Whereas Longmire et al. [15] observed the production of outward-spreading streamwise vortex pairs at the peaks but inward-spreading streamwise vortex pairs at the troughs, New et al. [19] found outward-spreading streamwise vortex pairs formed at both peak and trough locations. Closer inspection of the flow visualization images for both studies revealed that the flow differences may be due to Reynolds number effects, different peak and trough geometries, or a combination of both. For instance, the Reynolds number used for the turbulent air jet studied in [15] was $Re = 19,000$, in contrast with $Re = 2000$ for the laminar water jet used in [19]. Significant differences in the jet shear layers between the two different jets may also contribute towards the flow differences between the two studies. Additionally, the IO nozzles used in [15] were machined off to produce relatively sharp peaks and troughs, whereas for the IO nozzles used in [19], V-shaped cuts were machined on the nozzle to result in two smooth continuous peaks and two sharp discontinuous troughs. It is not inconceivable that smooth or sharp designs of the peaks and troughs may lead to significant alterations to the resultant flowfields as well. Hence, to investigate the issue further and gain deeper insights into the flow problem, the present study will seek to study how smooth and sharp configurations of peaks and troughs will affect the overall flow behavior at laminar and turbulent jet flow conditions. To accomplish that, two different types of nozzles will be used in this study: A nozzle with V-shaped cuts producing sharp troughs and smooth peaks (known as V-notched jets hereafter), and another nozzle with A-shaped cuts producing sharp peaks and smooth troughs (known as A-notched jets hereafter).

An interesting aspect of the earlier qualitative flow visualization studies [15,19] is that notched nozzle jets may exhibit "axis-switching" behavior similar to that observed in noncircular jets, particularly in elliptic jets, because the vortex rings appear to bend after some distance downstream away from the nozzles. Support for this notion comes from two considerations: Firstly, flow visualization images show that the vortex rollups emerging from these nozzles due to inherent jet shear layer instabilities follow the contour of the nozzle lips and thus resemble bent elliptic vortex rings. These bent elliptic vortex rings are visually similar to those observed in previous studies [1,2,20] during the intermediate stages and could arguably lead to axis-switching behavior, despite the differences in the initial conditions between their studies and the present case. Secondly, laser cross-sectional views presented by [15,19] showed a slight elongation of the jet cross section along the trough-to-trough plane downstream of the nozzle, which lends further support to the existence of partial or full axis-switching behavior. However, limited experimental results then as well as the need to focus more on the understanding how the streamwise vortex pairs initiate and evolve meant that further investigations have to be carried out in a separate study. Hence, part of the present study will also seek to shed more light on the possibility of axis-switching behavior within the context of an experimental comparison between these two different nozzle configurations.

The present study is carried out to address three specific concerns: Firstly, to investigate the flow structures and any pertinent differences in the general vortex dynamics that may exist between laminar V- and A-notched nozzle water jets in low-Reynolds-number dye-visualization studies. Secondly, to compare quantitatively the resultant flowfields of turbulent V- and A-notched nozzle air jets at high Reynolds number in terms of centerline velocity and turbulence properties, downstream velocity profile developments, and jet widths, among others. Lastly, to collate any detectable qualitative and quantitative flow behavior that will lend support to the existence of axis-switching phenomenon. To facilitate better understanding, a circular reference nozzle will be studied alongside these two types of nozzles as well. Detailed descriptions of the V- and A-notched nozzle designs, flow visualization, and hot-wire anemometry setup will be provided in Sec. II to give the readers a good understanding of the experimental facilities. Results will be presented and their impact on the current understanding discussed in Sec. III before conclusions from the present study are given in Sec. IV.

II. Experimental Apparatus and Setup

A. Nozzle Designs

Figure 1 shows the design details of the V- and A-notched, as well as circular reference nozzles used for the present study. For a more meaningful comparison, the mean heights H of all nozzles were kept constant at $2D$ (20 mm). Unlike earlier studies, in which more importance was placed on the relative heights of the peaks and troughs, the designs of the present notches are based on the aspect ratio (AR) of the half-ellipse formed by each half of the notches. For example, line AB (see Fig. 1b) indicates half the nozzle lip when viewed in the peak-to-peak plane. When viewed perpendicular to the half nozzle lip, the lip traces the exact contour of half an ellipse. The design methodology for the A-notched nozzle is similar (see Fig. 1c) and the aspect ratios used in the ellipse in both cases are at a moderate ratio of 1.5:1 (AR = 1.5). Depending on how the notches are cut along the nozzle lips, a series of sharp/smooth peaks and troughs will be produced along the nozzle lips. V-notched nozzles will possess smooth peaks and sharp troughs, whereas A-notched nozzles will have sharp peaks and smooth troughs instead.

B. Flow Visualization

All experiments were carried out in the Fluid Dynamics Lab at Temasek Laboratories, National University of Singapore. For the flow visualization study, dye visualization was carried out in a recirculating vertical water tunnel having a 400×400 mm square base and 1.4 m high. To allow excellent optical access from almost any viewing direction, the water tunnel was fabricated entirely out of Plexiglas. To mount the jet apparatus onto the water tunnel, a circular opening exists in the middle of the square base such that the jet apparatus can be inserted and mounted securely. Water for the jet apparatus was channeled from a gravity-driven constant pressure water tank for more stable jet flows with the jet flow rates controlled using an inline throttle valve and an electromagnetic flow meter. Upon entering the jet apparatus, the jet fluid had to pass through a series of honeycombs, fine screens, and a 36:1 contraction chamber designed according to [21] for proper flow-conditioning purposes before exhausting into the water tunnel from the test nozzles attached

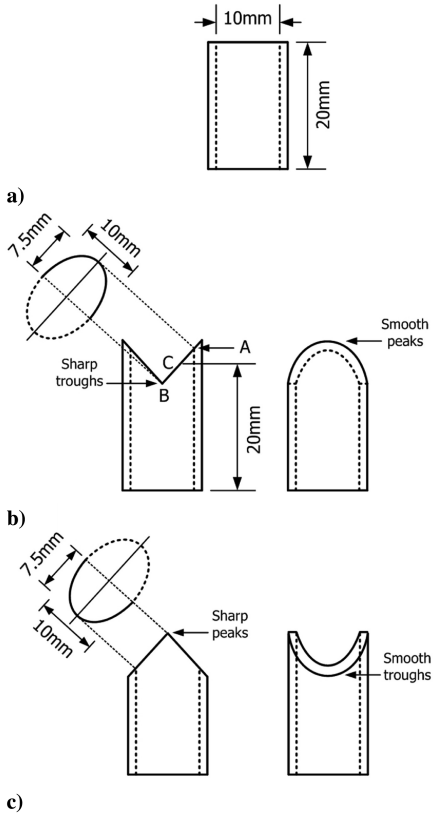

Fig. 1 Schematics of the a) circular reference nozzle, b) AR = 1.5 V-notched nozzle, and c) AR = 1.5 A-notched nozzle used in the present study. All nozzle internal diameters are 10 mm with the mean height *h* located at two jet diameters (20 mm) downstream of the nozzle bases.

to the end of the contraction chamber as shown in Fig. 2. According to earlier investigations [1,22], these flow-conditioning devices are able to produce jets with well-defined "tophat" or "flat" velocity profiles across a wide range of flow conditions. Hence, it would seem reasonable to assume similar velocity profiles for the jets used in the flow visualization study.

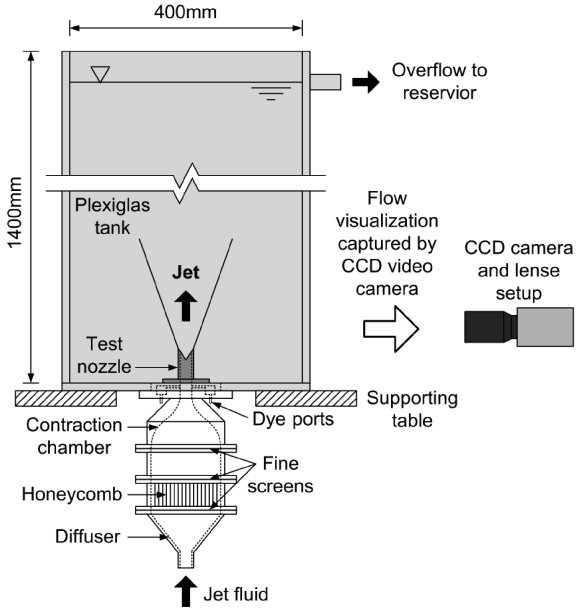

Fig. 2 Schematics showing the contoured water-jet apparatus with flow-conditioning devices, recirculating water jet, and Plexiglas tank setup, as well as CCD video camera and lens for flow visualization purposes used in the flow visualization study.

Although both unforced and forced flow conditions are carried out in the study, only the results for forced conditions will be discussed for brevity's sake as they are observed to produce similar but better organized coherent flow structures that ease flow interpretation [16,19,23], provided that the forcing is only strong enough to perturb the jet shear layer to initiate vortex rollups. For example, flow visualization images of forced and unforced jets presented in [19] revealed little qualitative flow structural differences between the two, with forced jets offering better understanding of the vortex flow developments by reinforcing the production of the small-scale streamwise vortex pairs. Forcing was imparted on the continuous jet for an additional pulsating flow component using a 200 W speaker-driven piston driven by a function generator before the jet fluid's entry into the jet apparatus. The magnitude of the forcing was adjusted such that the jet shear layers were just sufficiently perturbed to result in vortex rollups and the accuracy of the forcing was checked by recording small segments of videos and measuring the frequencies. No detailed measurements of the forced flows were carried out as the aim of creating the pulsating flows was not to study their effects on the nozzle flows but rather, to organize the flow structures better for flow interpretation. Forcing frequency was fixed at a Strouhal number of $St = 0.5$.

Lastly, all flow visualization experiments were recorded using a 25 frames-per-second frame-rate Sony DXC-990P color CCD video camera onto a Sony DVCAM recorder for subsequent playback analysis. Still images from the video recordings were then extracted using a frame-grabber card in a workstation for frame-by-frame analysis.

C. Hot-Wire Anemometry

All hot-wire anemometry experiments were carried out in an air-conditioned room with the temperature set at $25 \pm 0.5°C$ throughout the entire study. For the purpose of velocity and turbulence measurements, jet air supply was provided by an air compressor and passed through an air filter and dehumidifier before entering the jet apparatus. Figure 3 shows air entering the apparatus into a settling plenum before passing through a series of perforated sheets, honeycomb screens, fine steel grids, and eventually a 36:1 contraction chamber to straighten and condition the air jet. The design of the contraction chamber was also in line with the design rules laid out by [21]. The flow velocity of the jet was predetermined at 30 m/s and with the $D = 10$ mm diameter of the jet nozzles used, the corresponding Reynolds number was calculated to be approximately $Re = 20,500$ and close to that used by [15], in which $Re = 19,000$. At this Reynolds number, momentum thickness of the jet shear layer was calculated to be approximately $\theta/D = 0.025$ at $0.1D$ from the circular reference nozzle exit. Figure 4 shows a schematic of the coordinate system used during the hot-wire measurements. Note that $z/D = 0$ location corresponds to the mean height of both nozzles and resides in between the peak and trough heights. Because of the nature of the setup, hot-wire measurements were taken along a vertical direction with the nozzles rotated 90 deg where necessary to change the measurement plane.

Flow measurements were facilitated by the use of a single-channel Dantec CTA anemometer and a Dantec 55P16 single-normal hot-wire probe with an overheat ratio of 1.8. The present study did not attempt to differentiate between streamwise and cross-stream velocity components by using cross wires, but instead relied on the single-normal hot-wire probe to give integrated velocity signals regardless of flow direction. Although the use of a single-sensor hot-wire probe will give rise to significant biasing errors with the jet shear layers, it is adequate to be used for comparison purposes across the different nozzle types used here. Calibration of the hot-wire probe was carried out before each period of experiment and fitted to a fourth-order polynomial calibration curve as recommended by the manufacturer [24]. Voltage signals from the anemometer were channeled to a National Instruments NI-PCI6014 16-bit DAQ card in a workstation for differential-input data acquisition. Typically, signals were sampled at 5 kHz for 30 s period for a total of 150,000 data values at each sampling point. To ensure spatial accuracy, the

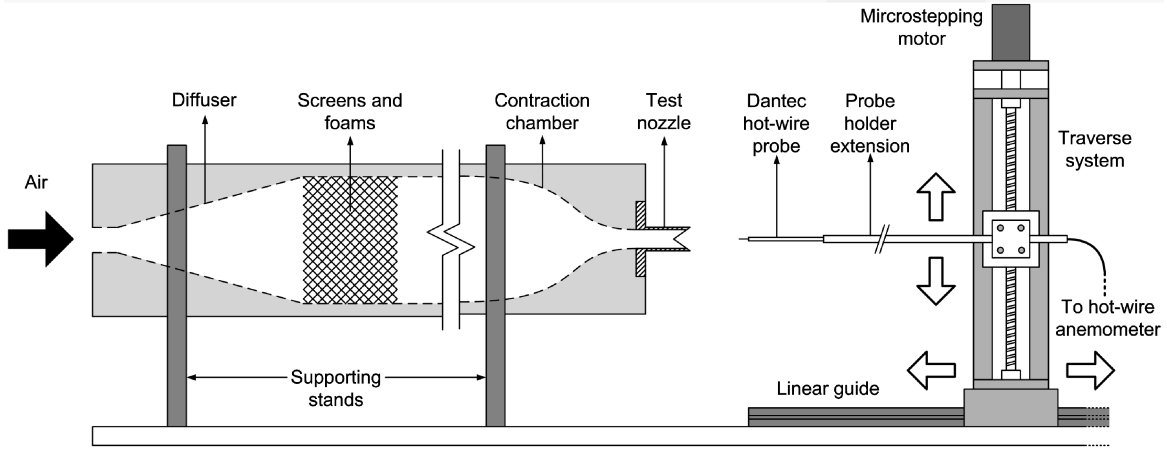

Fig. 3 Schematics of the contoured air-jet apparatus, automated traverse system, and hot-wire probe setup used in the velocity and turbulence measurement study. Signal from hot-wire probe was channeled to a DAQ card in a workstation, which in turn was used to coordinate the traverse system and automate the velocity measurement experiments.

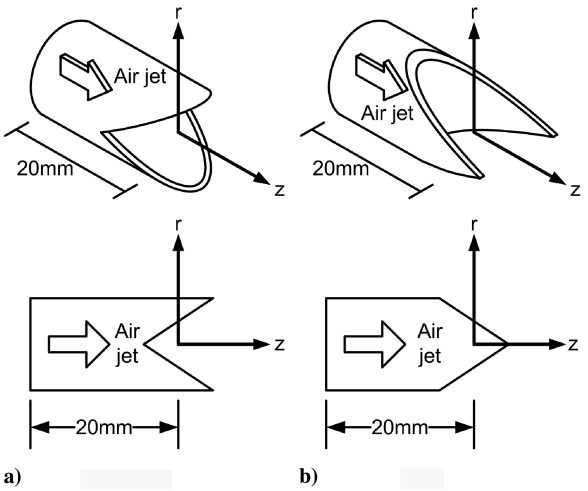

Fig. 4 Schematics of the coordinate systems used for hot-wire measurements on a) V-notched nozzle and b) A-notched nozzle. The coordinate system origin is located at the nozzle center and two jet diameters downstream from the bases of both nozzles.

hot-wire probe location was controlled by a two-axis CAN-bus controlled traverse mechanism and workstation (see Fig. 3). Before each measurement experiment, the hot-wire probe location was set to a fixed location corresponding to the nozzle center using a "homing" limit switch to ensure consistency. Each axis of the traverse consists of a 5-mm-pitch lead-screw driven by a microstepping motor and has a rated resolution of 25 μm. With all the hot-wire anemometer output, motor controllers, and sensors connected to the DAQ card, acquisition of hot-wire signals and motion of the traverse mechanism were entirely automated via the use of National Instruments' Labview program.

D. Experimental Uncertainties

Because flow visualizations were only used to identify the flow structures and their mutual interactions in the nozzle jet flows, uncertainties arising from the hot-wire velocity and turbulence measurements will be discussed here instead. Firstly, based on the prescribed jet flow velocity of 30 m/s, the maximum uncertainty in the jet flow velocity was determined to be approximately $\pm 3\%$ based on the air regulator and flow-metering device setup. Secondly, for jet velocity and turbulence profiles measurements across the jet nozzles, minimum cross-stream measurement intervals of 0.2, 0.4 and 1 mm were used when these measurements were taken at $0 \leq z/D \leq 2$, $2 < z/D \leq 5$, and $z/D > 5$, respectively. Based on a traverse system resolution of 25 μm, the traverse system resolution was calculated to be 1/8, 1/16, and 1/40 of the minimum measurement intervals. In terms of the jet nozzle dimensions, the traverse system resolution will be 0.25% of the nozzle diameter. Thirdly, during the hot-wire measurements, the hot-wire anemometer, hot-wire probe, and data-acquisition system were left on standby mode for a significant stretch of time (typically 1 h) before the actual experiments to stabilize the system. The use of a temperature-controlled room also minimized temperature variations that might impact the hot-wire measurements. To further reduce potential experimental uncertainties, an air dehumidifier was used to dry the air before its entry into the jet apparatus such that any errors caused by the limited presence of water vapor were minimized and could be neglected. Uncertainties were estimated from system testing carried out before the commencement of hot-wire anemometry study and indicated that combined uncertainties due to temperature variation, drift of the hot-wire system, and the data-acquisition system could be estimated to be no more than $\pm 2\%$, according to the procedures described in [24]. Based on the preceding figures, the total maximum uncertainty level was estimated to be approximately $\pm 3.6\%$.

III. Results and Discussion

A. Flow Visualization Results

To find out whether A-notched nozzle vortex dynamics differ from those of V-notched nozzles, sequential flow images of both V- and A-notched nozzle jets under forced conditions ($St = 0.5$) as viewed along the peak-to-peak (PP) and trough-to-trough (TT) planes are presented in Figs. 5–8. Forcing was used as it has been shown earlier [16,19,23] so that it organizes the coherent structures and hence facilitates a better understanding of the dominant flow structures. To avoid any extraneous flow structures that may result because of excessive forcing, the amplitude of forcing was adjusted to be just sufficient to perturb the jet shear layer to become unstable [16,19]. The sequence of the flow images is arranged such that the first flow image shows the initial manifestation of instability along the jet shear layer under the forcing imparted with subsequent flow images at 40 ms apart. For a better understanding of the relationship between the evolution phase of the flow structures and the forcing, timings of the flow images are normalized by the forcing period T such that the nondimensionalized times t^* are defined as $t^* = t/T$. Lastly, the flow visualization was accomplished by releasing colored dye slowly into the jet shear layer through a circumferential slit before it exited the nozzles, so that relevant developments along the jet shear layers could be better observed.

Figures 5 and 6 show the flow image sequences for the V-notched nozzle jet viewed normal to the PP and TT planes, respectively. It can be observed that under the perturbation of a particular instance of forcing, the jet shear layer became unstable with the instability taking after the outlines of the troughs and peaks. This indicates that the

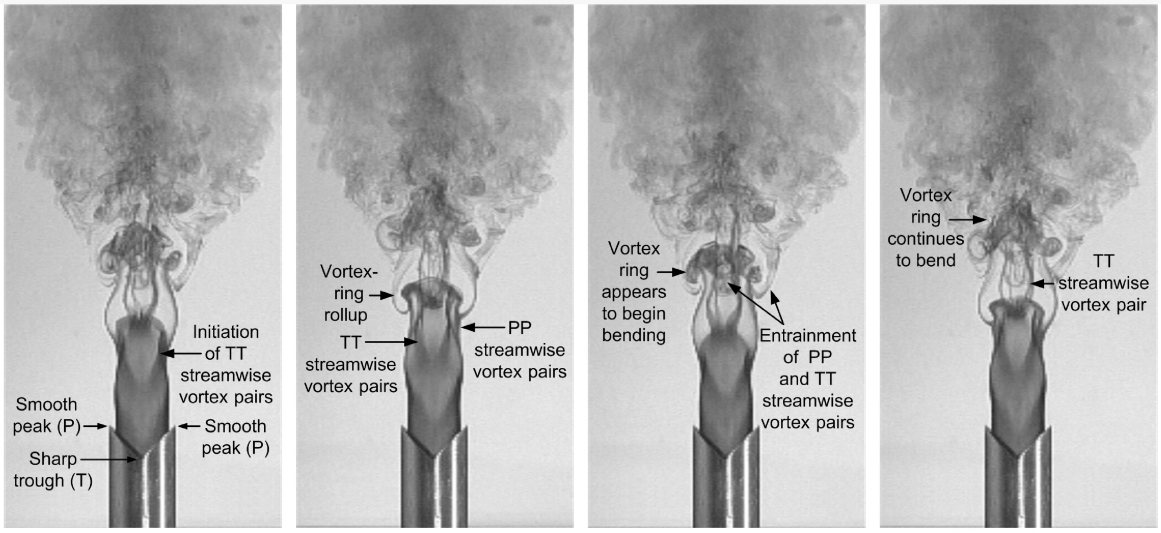

a) t*=0 b) t*=0.4 c) t*=0.8 d) t*=1.2

Fig. 5 Sequential flow visualization images for V-notched nozzle jet at $Re = 2000$, $St = 0.5$, from $t^* = 0$ to 1.2 at $t^* = 0.4$ intervals. Peaks and troughs are denoted as P and T, respectively, and hence streamwise vortex pairs formed at these locations are termed as PP and TT streamwise vortex pairs. The present viewing orientation is normal to the PP plane and shows how a typical TT streamwise vortex pair forms as a result of the deformation of the vortex filament due to the trough in a)–c), before it is entrained by the large-scale ring vortex shown in c). Bending of the large-scale ring vortex can be observed in c)–d) as well.

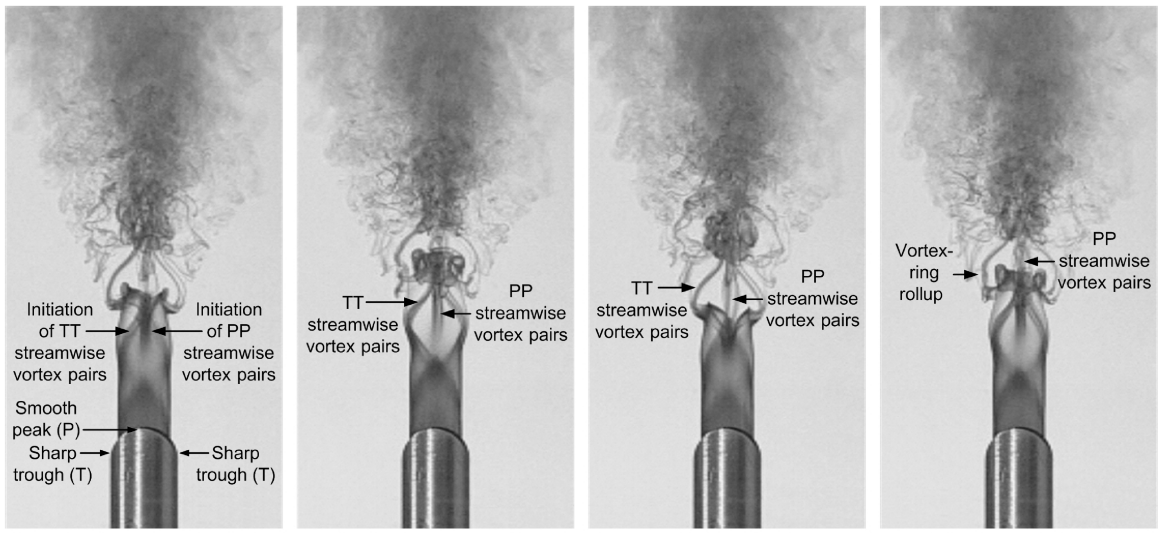

a) t*=0 b) t*=0.4 c) t*=0.8 d) t*=1.2

Fig. 6 Sequential flow visualization images for V-notched nozzle jet with similar flow conditions as with the case shown in Fig. 5 with the viewing orientation normal to the TT plane. In this view, it is shown how PP streamwise vortex pairs form from under the influence of the peak from a)–d). Similar to the TT streamwise vortex pair shown in Fig. 5, it is eventually entrained by the large-scale ring vortex in d), although no bending of the ring vortex is observed here.

instability would be partially aligned along the streamwise direction, and with the flow convection, streamwise vortex pairs were observed to initiate and form at both the trough and peak locations (TT and PP streamwise vortex pairs, respectively) in the first two flow images of Figs. 5 and 6. As the flow developed further with the rolling up of a large-scale azimuthal vortex ring, these streamwise vortex pairs were subsequently entrained as the vortex ring grew in size. New et al. [19] had shown earlier that these streamwise vortex pairs possess outwards-spreading rotation sense, regardless of whether they are formed by the peaks or troughs. Furthermore, they did not lose their coherency despite being entrained by the vortex ring but instead, earlier evidences showed that they "ride" upon the outer peripheral of the vortex ring. Perhaps most intriguingly, as the vortex ring evolved further downstream as shown in Fig. 5, it began to undergo a "bending" behavior at three to four jet diameters from the nozzle exit where sections of the vortex ring at the peak locations were located upstream of the vortex-ring sections at the trough locations (see Figs. 5c and 5d). However, inspections of Fig. 6 did not reveal such a bending behavior at corresponding stages. This observation indicates that deformations of the vortex rings may lead to limited or partial "axis-switching" phenomenon further downstream.

On the other hand, Figs. 7 and 8 show the flow image sequences for the A-notched nozzle jet viewed normal to the PP and TT planes, respectively. Note that in this case, the peaks were sharp instead of smooth and vice versa for the troughs. Despite the differences in the peak and trough configurations between the V- and A-notched nozzle jets, it appears from the flow images that the general vortex dynamics are similar. Again, flow images captured normal to the PP and TT planes revealed similar streamwise vortex pairs to be formed at both the peak and trough locations with the formation of the azimuthal vortex ring entraining them at subsequent stages. In fact, the flow similarity extends to the bending of the vortex ring

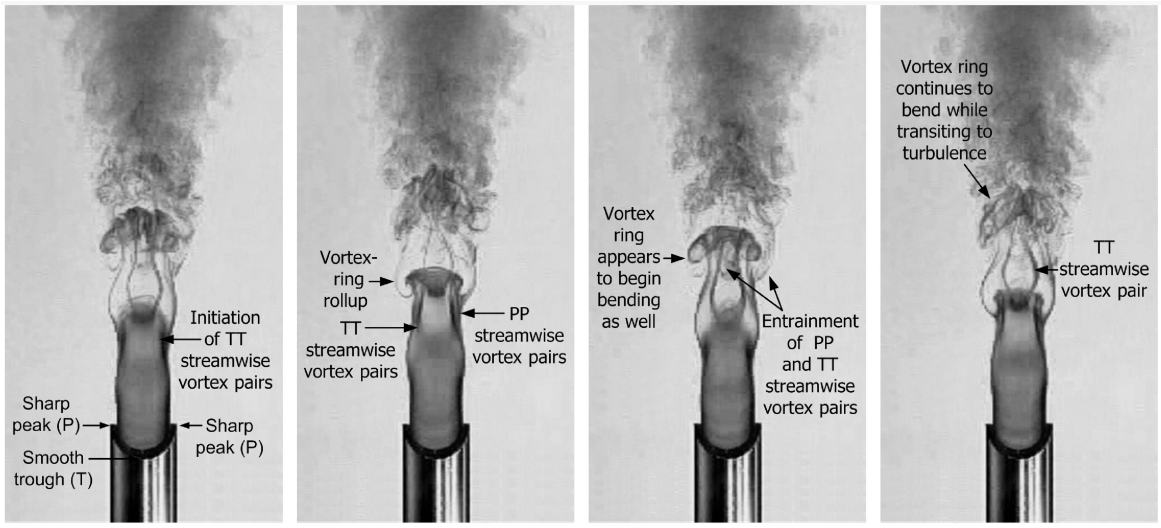

Fig. 7 Sequential flow visualization images for A-notched nozzle jet at $Re = 2000$, $St = 0.5$, from $t^* = 0$ to 1.2 at $t^* = 0.4$ intervals. The present viewing orientation is normal to the PP plane and shows that the formation and structure of the resultant TT streamwise vortex pair are very similar to that produced by the V-notched nozzle (see Fig. 5), including its entrainment and the bending of the large-scale ring vortex.

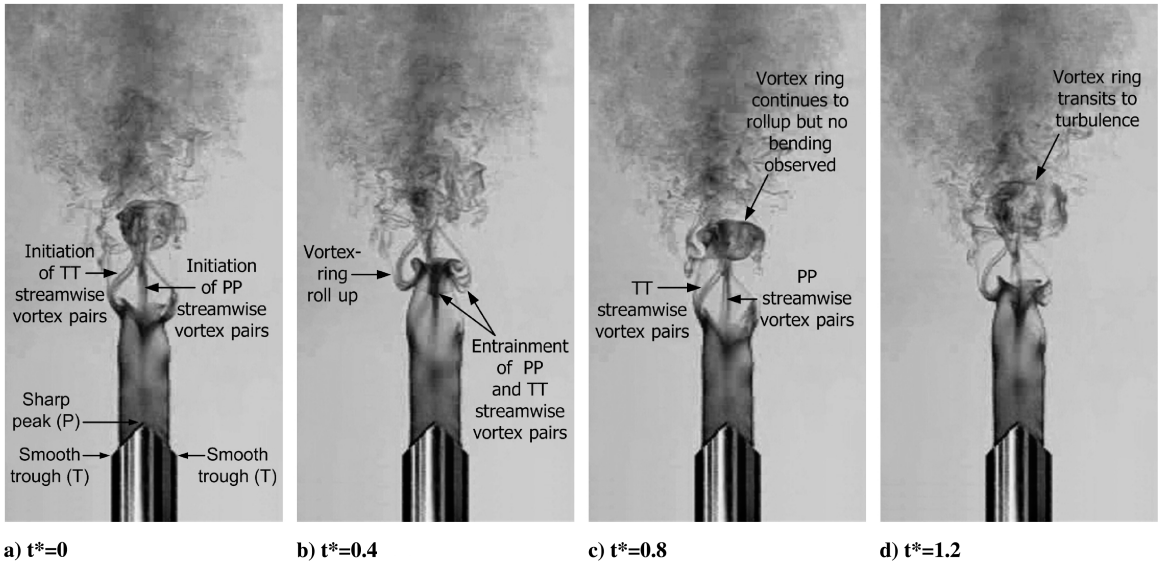

Fig. 8 Sequential flow visualization images for A-notched nozzle jet at $Re = 2000$, $St = 0.5$, from $t^* = 0$ to 1.2 at $t^* = 0.4$ intervals. Comparison with Fig. 6 reveals that the resultant PP streamwise vortex pair here is largely similar to that formed by V-notched nozzles and entrained by the large-scale ring vortex. Furthermore, no bending of the ring vortex is observed as well.

previously detected in the V-notched nozzle jet as well, as shown in Figs. 7c and 7d. Therefore, it appears that for a design aspect ratio of AR = 1.5, the vortex dynamics for laminar V- and A-notched nozzle jets under forced conditions bear very close resemblance with each other, and that the flow model presented by [19] for a V-notched nozzle jet will be largely applicable to a A-notched nozzle jet as well (see Fig. 9, in which the flow model is reproduced from [19]). In this case, physical geometrical differences between sharp and smooth peaks/troughs may not be sufficient to influence the flowfields to an extent where the dominant flow structures such as the streamwise vortex pairs and azimuthal vortex rings will be significantly affected. However, the question remains as to whether the general flow similarities between the two cases are due to the low aspect ratio or the laminar state of the jet flows used, which may be resilient against any influence brought about by the change in the peaks' and troughs' "sharpness."

Regardless of whether the general flow similarity observed during flow visualization was due to the aspect ratio or Reynolds number used, it remains interesting that the vortex rings emanating from these nozzles are observed to undergo bending as they convect downstream for both V- and A-notched nozzle jets. For a better inspection of the bending behavior in relevant flow images, Fig. 10 shows close-up views of the vortex rings normal to the PP plane observed to be undergoing bending behavior in V- and A-notched nozzle jets, respectively, with the observed bending curvature indicated by the dashed lines. Video playback indicated that the vortex rings in both cases began bending at approximately three to four jet diameters away from the nozzle exit shortly after they were formed in both cases. Most significantly, the vortex rings were bent such that portions of filaments corresponding to trough locations were further downstream than those corresponding to the peak locations, that is, opposite to the overall contours of the nozzle notches. The argument for axis-switching behavior to arise from these vortex deformations is credible, because it can be deduced that any vortex rings emanating from them will resemble "prebent" elliptic vortex rings as pointed out earlier. In fact, cross sections of the jet under similar flow conditions in an earlier study [19] revealed that the cross-sectional shape of the vortex rings changes from an initially

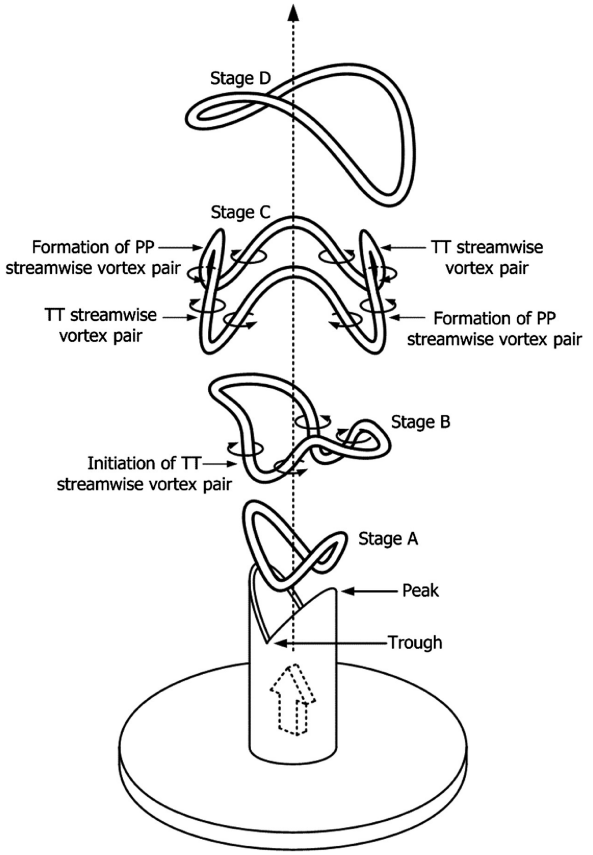

Fig. 9 Flow model proposed for a laminar indeterminate-origin V-notched nozzle jet suggests that the formation of the streamwise vortex pairs may be explained by the deformation of the vortex lines caused by the corresponding peaks and troughs (reproduced from New et al. [19]).

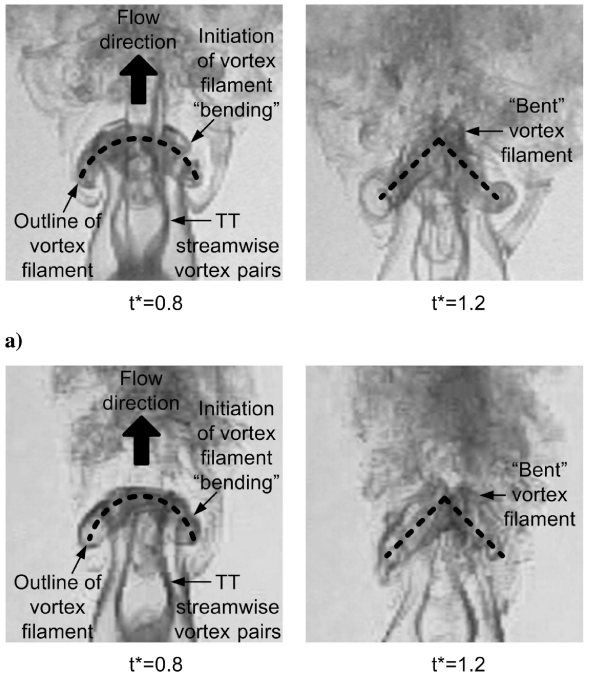

Fig. 10 Close-up views of consecutive flow visualization images at $t^* = 0.4$ apart ($t^* = 0.8$ and 1.2) for a) V-notched and b) A-notched nozzles viewed normal to PP planes reveal that bending of the vortex filaments occurs regardless of the peak/trough configuration with a large visual resemblance between the two cases. Outlines of the vortex filaments are shown to highlight the bending.

round shape to that of a round-edged square shape before the onset of its bending. In their studies on elliptic jets, Hussain and Husain [1] and Gutmark and Ho [20,25] have shown that even in initially flat elliptic vortex rings, unequal vortex stretching and induced velocities along the vortex filaments are able to lead to persistent switching of the elliptic vortex-ring major and minor axes as they convect away from the jet exit. The favorable nozzle designs used here should, in theory, accentuate some if not all of these effects despite inherent geometrical differences between notched and flat nozzles. This is further supported by the observation that the states of the vortex rings from V- and A-notched nozzle jets shown in Fig. 10 are similar to intermediate stages of axis-switching behavior observed in free elliptic jets studied by these earlier investigations. However, it should be pointed out here that it is unlikely that the deformed vortex rings will lead to exact axis-switching behavior observed in free elliptic jets. Instead, it is more likely that the axis-switching phenomenon in notched jets will be of a limited form and specific to the exact geometrical design, as well as being influenced by the existence of the streamwise vortex pairs along the peripheral regions of the vortex rings, the extent to which is still not clear. Nonetheless, due to the difference in scale between the vortex rings and the streamwise vortex pairs, it is probable that limited axis-switching behavior from the vortex rings will be largely responsible for the changes to the gross shape of the jet cross section, whereas the streamwise vortex pairs will lead to localized distortions to the peripheral regions of the jet cross sections.

B. Velocity and Turbulence Measurements

In the preceding section, flow visualization results have shown largely similar vortex dynamics for V- and A-notched nozzle jets at low Reynolds number, and suggest that the bending of the large-scale vortex rings may result in deformations to the gross shape of the jet cross sections, caused possibly by limited axis-switching behavior. This prompted a follow-up investigation using hot-wire anemometry which will be described in detail here. Unlike the case for the flow visualization study where laminar forced jet flows were used, the Reynolds number of the free nozzle jets used for hot-wire measurements was much higher at $Re = 20,500$, which represented fully turbulent jet flows. In contrast to the preceding section, the primary aim here is to discern any bulk flow differences in terms of flow velocities, velocity profiles, and turbulence levels when the two type nozzle types are compared at a much higher Reynolds number because no significant flow differences were found at low Reynolds number testing. The larger length- and time-scales in low Reynolds number experiments carried out earlier might have prevented the geometrical differences in the peaks and troughs to manifest their effects. On the other hand, it is difficult to detect the turbulent flow structures through flow visualization due to the much smaller length- and time-scales, hence quantitative hot-wire measurements were used here instead. Furthermore, the much thinner air jet shear layers and small length-scale flow structures are likely to be more sensitive towards whether the peaks and troughs are sharp or smooth. Although the flow phenomena for high Reynolds number flows may not be directly linked to those for low Reynolds number flows, some similar flow trends could be directly or indirectly detected if the underlying basic flow mechanisms persist. For instance, rather than to elucidate further the role of large-scale vortex ring bending and deformation in this case (which would not be easy), hot-wire measurement results will be used to detect any gross effects that could result from that behavior such as distortions to the jet cross sections. Nevertheless, it should be noted here that care should be taken when collating the results between the flow visualization and hot-wire studies.

1. *Centerline Velocity and Turbulence Characteristics*

Figure 11 shows the centerline velocity and turbulence intensity profiles for the circular reference, V- and A-notched nozzle jets between $z/D = 0$ and 50 from the nozzle mean height location. The centerline velocities are normalized by the prescribed exit velocity U, whereas the turbulence intensities are normalized by the

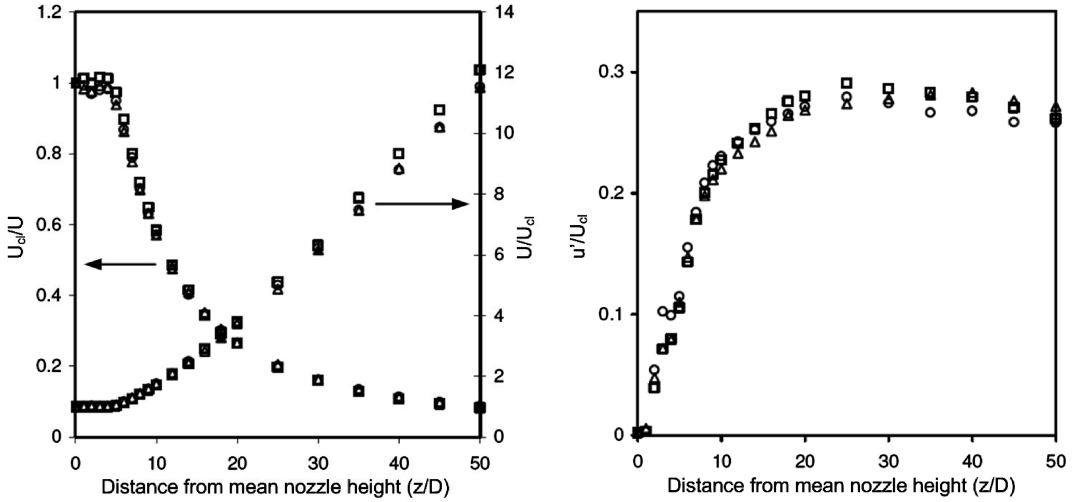

a) Centerline velocity profiles b) Centerline turbulence levels

Fig. 11 Comparisons of centerline velocity profiles and centerline turbulence levels between circular reference, V- and A-notched nozzles from $z/D = 1$ to 50 (○–Circular reference, □–V-notched, and △–A-notched). Centerline velocities U_{cl} are nondimensionalized by the mean jet velocity U, whereas centerline turbulence levels u' are nondimensionalized by the centerline velocities U_{cl} taken at the same measurement locations.

time-averaged jet centerline velocities at their respective measurement locations, U_{cl}. As shown in Fig. 11a, the centerline velocity profiles for all three nozzle configurations lie very close to one another, although there are some subtle differences that can be discerned. For instance, near-field centerline velocities for the V-notched nozzle are consistently higher over both the circular and A-notched up to $z/D = 16$ location and suggest slightly higher resilience against erosion of the potential core over the other two nozzles. On the other hand, A-notched nozzle jet centerline velocity decay did not differ significantly from the circular nozzle jet. Their potential core lengths measured approximately between four and five jet diameters before they were fully eroded and the centerline velocities decreased drastically thereafter. In the far field where centerline velocities tend towards an asymptotic level, the V-notched nozzle jet has slightly lower centerline velocities than the circular and A-notched nozzle jets. On the other hand, circular and A-notched nozzle jets have very close centerline velocities within the same region. As for the centerline turbulence intensities shown in Fig. 11b, they also appear to share largely similar trends as well, reaching maximum levels of approximately $u'/U_{cl} = 0.28$–0.29 at various downstream locations. However, it should be noted here that for the circular and V-notched nozzles, maximum turbulence intensities occur at $z/D = 25$, whereas for the A-notched nozzle, the maximum level occurs significantly further downstream at $z/D = 40$.

2. Half-Jet Velocity Profiles

To investigate how smooth and sharp peaks/troughs affect the quantitative aspects of these nozzle jet flows, Figs. 12 and 13 show half-jet velocity profile comparisons between V- and A-notched nozzles along PP and TT planes, respectively, from $z/D = 1$ to 5. The half-jet velocity profiles were taken at various cross-stream locations by the hot-wire probe starting from the jet nozzle exit center point ($r/D = 0$) up to $r/D = 2.8$, depending on the exact configuration. All the velocity profiles are normalized by the centerline velocities at their respective measurement locations. Although velocity data are available up to $z/D = 28$, differences between the velocity profiles of the three different nozzle types became insignificant beyond $z/D = 5$ and are not shown here for the sake of brevity. Hence, the velocity measurements within this range of downstream locations will provide a good understanding of the influences to the velocity profiles due to the peak/trough geometrical differences in the near-field region. For comparison's sake, similar velocity profiles obtained for the circular nozzle are included in the figure as well.

In Fig. 12, in which the effects of smooth and sharp peaks are compared, it can be observed that the jet velocity profiles along smooth peak locations did not decay as much as those along the sharp peak locations up to $z/D = 3$, after which the trend reversed and the former appeared to be decaying slightly faster than the latter. This

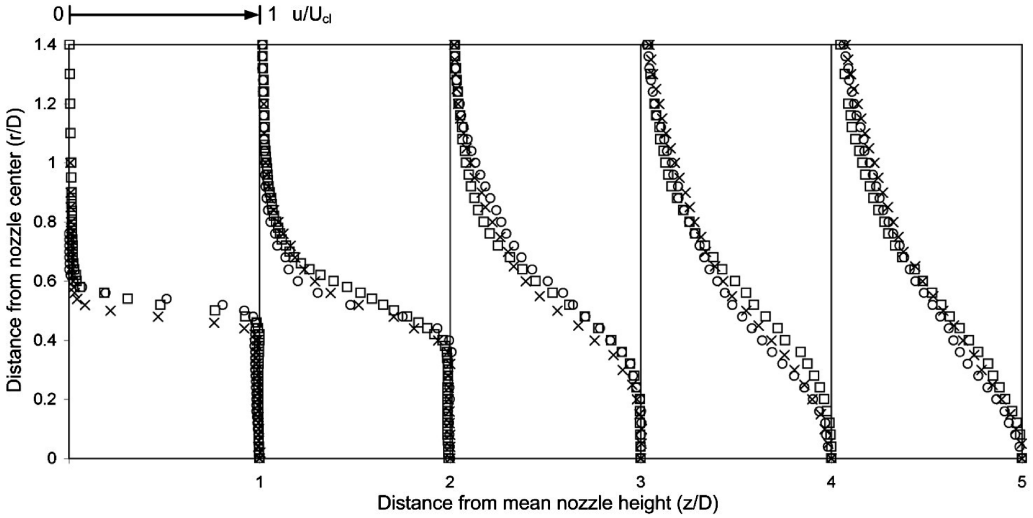

Fig. 12 Comparisons of half-jet velocity profiles between circular reference, V- and A-notched nozzles taken along PP planes from $z/D = 1$ to 5 show the effects due to smooth and sharp peaks (□–circular nozzle, ○–smooth, ×–sharp).

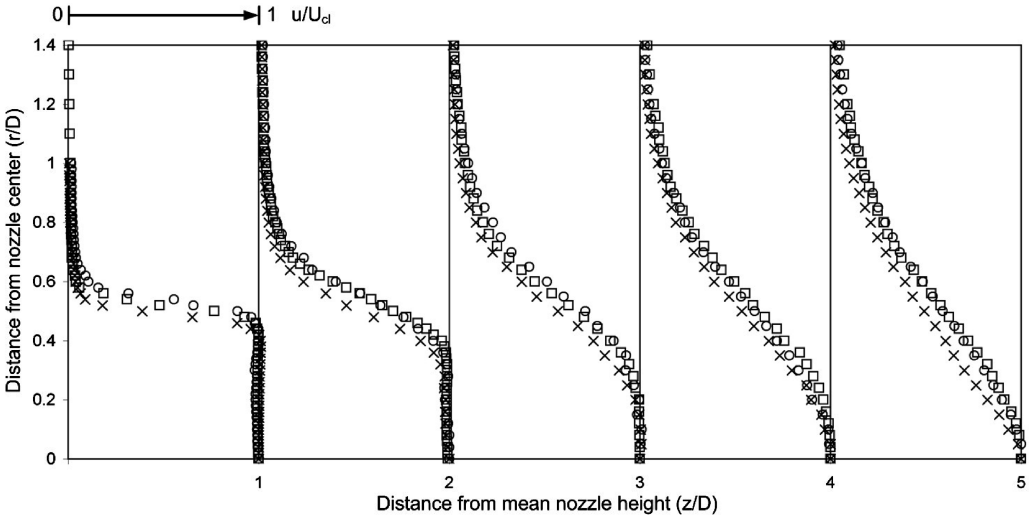

Fig. 13 Comparisons of half-jet velocity profiles between circular reference, V- and A-notched nozzles taken along TT planes from $z/D = 1$ to 5 show the effects due to smooth and sharp troughs (□–circular nozzle, ○–smooth, ×–sharp).

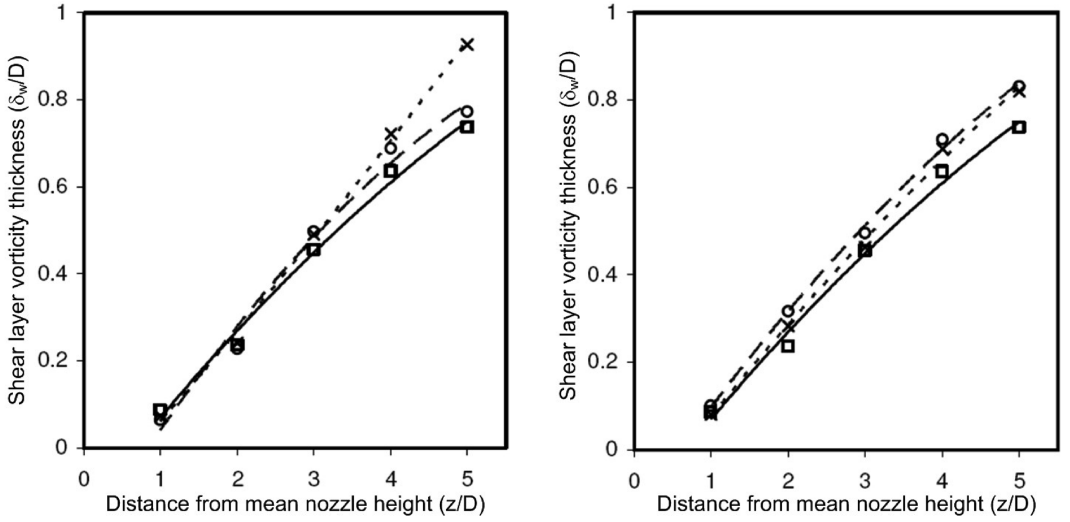

a) Smooth and sharp peaks **b) Smooth and sharp troughs**

Fig. 14 Comparisons of shear layer vorticity thicknesses between smooth and sharp peaks and troughs (□–circular reference, ○–smooth, ×–sharp).

results in smooth peaks having wider jet profiles over sharp peaks up to $z/D = 3$ but narrower jet profiles further downstream until $z/D = 5$. This can be explained by the lower turbulence levels registered at smooth peak locations when compared to sharp peak locations until $z/D = 3$ as shown in Fig. 15, where the turbulence measurements were taken at $r/D = 0.5$ (more details on turbulence levels will be discussed later). This indicates that smooth peaks result in stronger resilience against shear layer "erosion" over sharp peaks and may be a result of the difference in the nature of the streamwise vortex pairs produced by these two dissimilar peaks. Note that in Fig. 12, the velocity profiles for the circular nozzle within the first three jet diameters from the nozzle mean height location lie somewhat within those described by the smooth and sharp peaks, where they are wider than those of the sharp peaks but narrower than those of the smooth peaks. From $z/D = 4$ onwards, velocity profiles at both smooth and sharp peaks locations are "flatter" than those of the circular nozzle. On the other hand, Fig. 13 shows a comparison of the effects resulting from smooth and sharp troughs. It can be observed that smooth configuration of the troughs appears to achieve consistently wider half-jet velocity profiles over those resulting from sharp configurations from $z/D = 0$ to 5. Similarly also is the observation that velocity profiles for the circular nozzle lie within those of smooth and sharp troughs within the first three downstream locations. Furthermore, it bears to note that throughout the range shown in Fig. 13, velocity profiles at sharp troughs remained flatter than those at smooth troughs.

To sum up the significance of the observations in Figs. 12 and 13, sharp peaks and troughs consistently result in faster erosion of the velocity profiles compared to the reference circular nozzle taken along PP and TT planes, respectively. On the other hand, smooth peaks and troughs led to a small increase in the jet widths and hence velocity profiles as compared to the reference circular nozzle along their respective planes in the first jet diameter downstream away from the nozzle exit. Further away from the nozzle exit, however, their jet widths and velocity profiles subsequently fell below those of the circular nozzle. Hence, all peaks and troughs, regardless of whether they are smooth or sharp, are able to promote faster erosion of the nozzle jet shear layers.

3. Shear Layer Vorticity Thicknesses

The availability of the time-averaged velocity profiles also provides an opportunity here to compare the characteristics of the shear layer vorticity thicknesses (δ_w) between the three different nozzles. Figure 14 shows the comparisons between smooth and sharp configurations of peaks and troughs against each other as well as the circular reference nozzle. To arrive at the shear layer vorticity thicknesses, the centerline velocities U_{cl} were divided by the maximum velocity gradient (dU/dr) derived by applying a moving

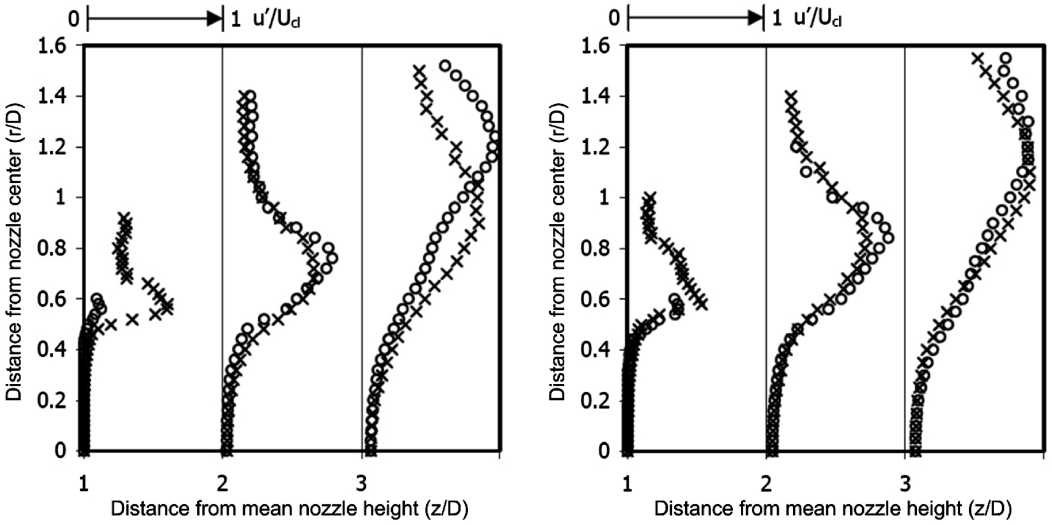

Fig. 15 Comparisons of turbulence intensity levels for V- and A-notched nozzles along PP and TT planes from $z/D = 1$ to 3 (○–PP plane, ×–TT plane).

system of three-point-derivatives on all the data points along the velocity profiles for consistency and comparison with [16]. In Fig. 14a, in which smooth and sharp peaks are compared against the circular reference nozzle, it can be observed that the circular reference nozzle has the smallest shear layer thickness throughout the measurement range. The shear layer thicknesses for the three different configurations did not differ from one another until $z/D = 2$, where both peak configurations began to increase their shear layer thicknesses faster than the circular reference nozzle. Even then, at $z/D = 3$ the rate of shear layer growth for smooth peak configuration began to drop below that of the sharp peak configuration, which continued to increase almost linearly up to $z/D = 5$. Hence, at $z/D = 5$, sharp peak configuration possessed the thickest shear layer vorticity thickness, followed by smooth peak configuration and circular reference nozzle, respectively.

In Fig. 14b, however, in which smooth and sharp troughs are compared against the circular reference nozzle, the shear layer thickness curves are found to share relatively similar growth trends. Not surprisingly, circular reference nozzle possessed the smallest shear layer thickness among the three nozzles. The shear layer thickness growth for the troughs appears to be less sensitive to the exact smooth/sharp configuration than the case for the peaks, where the curves for smooth and sharp troughs are observed to be very close. In fact, the result suggests that they almost converge upon each other at $z/D = 5$. However, upon closer inspection the shear layer thicknesses for smooth trough remain slightly higher than those for sharp troughs throughout this figure. In terms of increasing enhanced flow events along the shear layer and thereby leading to its thickness growth, sharp peaks and smooth troughs appear to perform better in the near-field region.

4. *Turbulence Characteristics*

To understand the effects of the peak and trough configurations on the turbulence intensities in the near-field region, Fig. 15 shows the overall comparisons of the half-jet turbulence intensity distribution up to $z/D = 3$. Because of significant bias in single-sensor hot-wire measurements, these measurements should be used for relative comparison purposes and treated as so hereafter. For the case of the V-notched nozzle, the turbulence level started out significantly higher in the shear region along the TT plane than the PP plane, with peak turbulence levels of approximately $u'/U_{\mathrm{cl}} = 0.60$ and 0.13, respectively, at $z/D = 1$. However, peak turbulence levels for both planes were comparable from $z/D = 2$ onwards with the PP plane reaching slightly higher levels. Similar trends can also be observed in Fig. 15b for the case of the A-notched nozzle, where higher peak turbulence level existed along the TT plane at $z/D = 1$ but reached comparable levels for both planes from $z/D = 2$ and 3 onwards. However, it should be noted that for the A-notched nozzle, the peak turbulence level along the PP plane was significantly higher than that registered along the similar measurement plane for the V-notched nozzle at the $z/D = 1$ location. For instance, the peak turbulence level along the PP plane of A-notched nozzle at $z/D = 1$ was measured to be approximately $u'/U_{\mathrm{cl}} = 0.37$ as compared to $u'/U_{\mathrm{cl}} = 0.13$ for the V-notched nozzle under similar conditions. All other peak turbulence levels were found to be comparable between the V- and A-notched nozzles. Hence, it appears that for this particular design aspect ratio of AR = 1.5, a change in the peak geometry from a smooth contour to a sharp and discontinuous one will lead to increase in the peak turbulence levels along the shear regions. In contrast, the peak turbulence levels downstream remained mostly independent of whether the trough contour is smooth or sharp. It should be mentioned here that the measured turbulence levels appear to be relatively high and very likely due to the biasing effects of the single-sensor hot-wire in highly turbulent flows.

5. *Half-Jet Width Comparisons*

As for the effects on the average jet-spread due to different peak and trough configurations on both near- and far-field regions, Fig. 16 shows the half-jet widths normalized by the jet diameter determined from half-jet velocity profiles obtained between $z/D = 1$ and 28 with the uncertainty levels indicated by error bars. Half-jet widths are defined here as the radial distances from the nozzle exit center where the averaged local velocities are half that of the averaged jet centerline velocities at various downstream locations $(r/D)_{\bar{u}/U_{\mathrm{cl}}} = 0.5$. In Fig. 16a, in which the comparison between smooth and sharp peaks is shown, sharp peaks consistently achieved a slightly larger jet width over smooth peaks from $z/D = 4$ onwards. However, within the range of downstream locations investigated, the discrepancy in jet widths diminished gradually further downstream with both type of peaks resulting in almost similar jet widths. On the other hand, Fig. 16b shows that the difference in jet widths between smooth and sharp troughs is consistent and does not appear to diminish at the furthest downstream locations considered in the present study. These results support the earlier conjecture that sharp peaks and smooth troughs perform better over their counterparts in terms of increasing jet spreads, although the improvements may not be very significant.

Figure 17 shows the comparisons of half-jet widths of V- and A-notched nozzles between PP and TT plane for $z/D = 1$–28. Similar to Fig. 16, error bars associated with the estimated uncertainty levels are indicated in Fig. 17 as well. Such a comparison not only allows one to understand how jet width along one axis changes relatively to another axis, it also reveals whether distortions to jet boundaries and cross sections have occurred. It is also possible to detect if axis-switching behavior exists in the jet flow where axis-switching

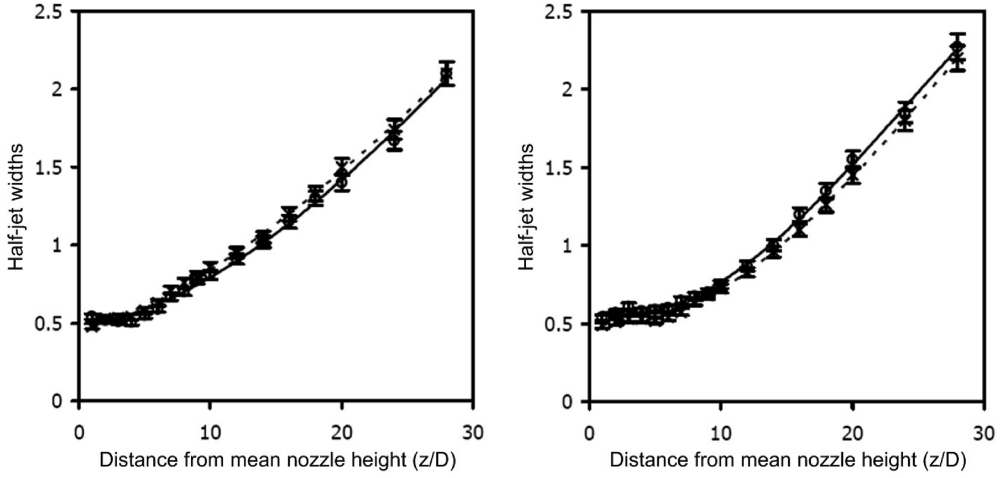

a) Smooth and sharp peaks **b) Smooth and sharp troughs**

Fig. 16 Comparisons of half-jet widths for smooth and sharp peaks and troughs as measured along PP and TT planes, respectively, from $z/D = 1$ to 28 (○–smooth, ×–sharp).

locations can be deduced from the "crossover" points between the two curves, although it should be mentioned here that the axis-switching phenomenon may be in a sense limited. Nonetheless, if axis-switching locations were detected, it will support the notion that the vortex dynamics of notched nozzle jets can be satisfactorily model after bent elliptic vortex rings as proposed by New et al. [19], because elliptic vortex rings are known to lead to such axis switching. In Fig. 17a, in which the V-notched nozzle was considered, two possible axis-switching locations could be located at approximately $z/D = 2.5$ and 19. On the other hand, for Fig. 17b, in which the A-notched nozzle was considered, another two possible crossover points could be located at approximately $z/D = 4.5$ and 18. The proximity of the two axis-switching locations in both V- and A-notched nozzle jets lends support to the earlier flow visualization images and suggests that their underlying dominant vortex dynamics may share similar behavior even in high-Reynolds-number flows. However, it is worthwhile to mention here that the use of single hot-wire probe meant that there is a small degree of uncertainty in the exact locations of these crossover points.

Compared to the studies on free elliptic jets of AR = 2 in [1,25], the two axis-switching locations for each of the two nozzles considered here are in good agreement with those of the elliptic jets. For example, Ho and Gutmark [25] observed three axis-switching locations at $x/a = 3$, 28, and 38, where x denoted the downstream distance from the elliptic jet exit and a was the half major axis diameter used in their study. Using similar normalizing terms as them, the axis-switching locations for the V-notched nozzle jet here will be located approximately at $x/a = 3.3$ and 25, whereas they will be located approximately at $x/a = 6$ and 24 for the A-notched nozzle jet. These locations are in good agreement with the first two locations found by Ho and Gutmark [25], considering the difference in the initial nozzle geometries (aspect ratio and presence of notches) and vorticity distributions. The present measurement range did not allow verification of the third axis-switching location at $x/a = 38$. Despite the general agreement on the axis-switching phenomenon between the present notched nozzles and free elliptic jets in terms of occurrence locations, one should bear in mind that the initial conditions for notched nozzles are significantly different from those of free elliptic jets. Therefore, the overall vortex dynamics and flow mechanisms for notched nozzles and free elliptic jets are unlikely to be the same, although it will be conceivable that they will share certain flow similarities.

6. *Remarks*

As a concluding remark, in interpreting the flow visualization and hot-wire measurement results presented earlier, it should be noted that the aim of the flow visualization study is to give the readers a better understanding of the fundamental vortex dynamics, in particular the observations that bending of the large-scale vortex rings occurs consistently in both nozzle types. On the other hand, hot-wire measurements are primarily used to quantify the flow properties in question, although they interestingly revealed that crossover points exist in comparisons between the jet widths taken along the PP

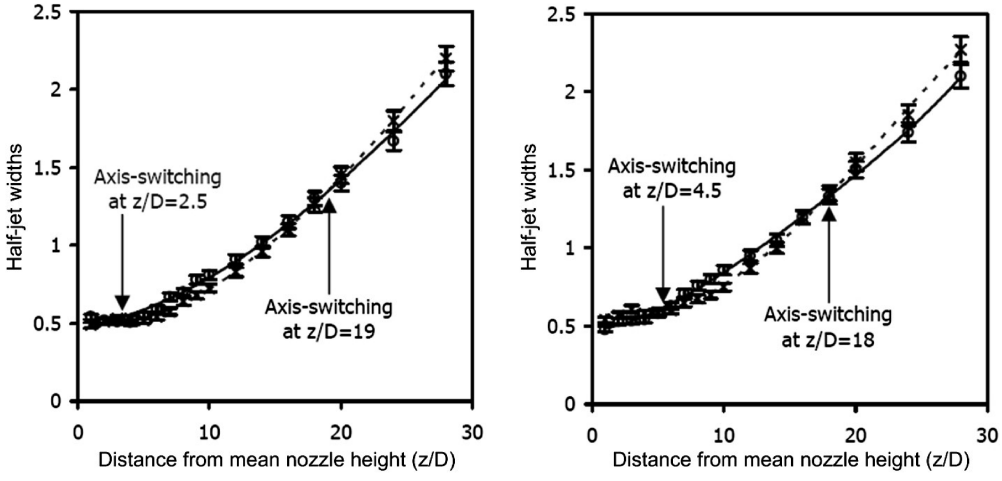

a) V-notched nozzle **b) A-notched nozzle**

Fig. 17 Comparisons of half-jet widths for V- and A-notched nozzles along PP and TT planes from $z/D = 1$ to 28 (○–PP plane, ×–TT plane).

and TT planes for each of the two nozzle types. Although the difference in the Reynolds numbers between the flow visualization and hot-wire measurements prevents direct correlations between the two, they nonetheless suggest that some dominant features of the underlying flow mechanisms may be sufficiently robust to exist within a significant Reynolds number range, especially if they involve large-scale vortex rings (similar to free elliptic jets). Obviously, the flow mechanisms between low and high Reynolds number nozzle jet flows will not be exact due to the significantly smaller length- and time-scales for high Reynolds number flows, which will lead to different flow behavior, in particular, the small-scale streamwise vortex pairs induced by the peaks and troughs. However, large-scale vortex rings, which are governed by the gross nozzle shape, should exhibit some common flow features despite the Reynolds number difference. Hence, it remains plausible that salient but yet persistent features due to the bending of the vortex rings observed during low Reynolds number flow visualizations, which indicates limited axis-switching, may be retained in high-Reynolds-number hot-wire measurements and manifested as axis-switching locations in jet-width comparisons.

IV. Conclusions

An experimental flow visualization and hot-wire anemometry study has been carried out on V-and A-notched nozzles of design aspect ratio AR = 1.5 to investigate the influence of smooth or sharp configurations for the peaks and troughs. Time-sequenced flow visualization images show that the formation of the large-scale ring vortices, small-scale streamwise vortex pairs, and their subsequent interactions for the two nozzle types are generally similar. As such, this suggests that the flow model proposed by New et al. [19] for V-notched nozzles should be applicable to A-notched nozzles as well, provided that the design aspect ratio remains moderate. Interestingly, flow visualization results revealed bending of vortex rings emanating from both types of nozzles and suggest distortions to the gross jet cross-sectional shape, possibly caused by limited axis-switching behavior resembling that observed in free elliptic jets.

Velocity measurements showed that sharp peaks resulted in wider jet widths over smooth peaks, but the difference decreased with increasing downstream distance from the nozzle exits. In contrast, jet widths along smooth trough locations were consistently wider than those along sharp trough locations throughout the range of downstream locations studied. Differences in peak turbulence levels caused by whether the peaks and troughs were smooth or sharp were restricted mainly to the immediate vicinities of the nozzle exit, where sharp peaks resulted in significantly higher turbulence levels than smooth peaks. Turbulence levels were found to remain approximately invariant regardless of trough configurations.

When half-jet widths along PP and TT planes were compared, crossover locations that indicate axis-switching behavior were detected and quantified for the first time in V- and A-notched nozzles. Two axis-switching locations were found for both V- and A-notched nozzles at $z/D = 2.5$, 19 and $z/D = 4.5$, 18, respectively, and agreed well with axis-switching locations of free elliptic jets observed by Ho and Gutmark [25]. However, due to the different initial flow conditions between the notched nozzle jets and free elliptic jets as well as the presence of the streamwise vortex pairs in notched nozzle jets, the vortex dynamics leading to axis switching for the two different scenarios will unlikely to be the same. Instead, the axis-switching behavior for notched nozzles is likely to be limited with the exact mechanism influenced by the presence of the streamwise vortex pairs.

Acknowledgments

The authors acknowledge the assistance in hot-wire anemometry measurements by K. S. Lim of Temasek Laboratories and the support by Directorate of Research and Development, Defence Science and Technology Agency, Singapore.

References

[1] Hussain, F., and Husain, H. S., "Elliptic Jets. Part 1. Characteristics of Unexcited and Excited Jets," *Journal of Fluid Mechanics*, Vol. 208, 1989, pp. 257–320.

[2] Gutmark. E. J., and Grinstein, F. F., "Flow Control with Noncircular Jets," *Annual Review of Fluid Mechanics*, Vol. 31, 1999, pp. 239–272.

[3] Zaman, K. B. M. Q., "Spreading Characteristics of Compressible Jets from Nozzles of Various Geometries," *Journal of Fluid Mechanics*, Vol. 383, 1999, pp. 197–228.

[4] Mi, J., Nathan, G. J., and Luxton, R. E., "Centreline Mixing Characteristics of Jets from Nine Differently Shaped Nozzles," *Experiments in Fluids*, Vol. 28, No. 1, 2000, pp. 93–94.

[5] Danaila, I., and Boersma, B. J., "Direct Numerical Simulation of Bifurcating Jets," *Physics of Fluids*, Vol. 12, No. 5, 2000, pp. 1255–1257.

[6] Reynolds, W. C., Parekh, D. E., Juvet, P. J. D., and Lee, M. J. D., "Bifurcating and Blooming Jets," *Annual Review of Fluid Mechanics*, Vol. 35, 2003, pp. 295–315.

[7] Bradbury, L. J. S., and Khadem, A. H., "The Distortion of a Jet by Tabs," *Journal of Fluid Mechanics*, Vol. 70, 1975, pp. 801–813.

[8] Reeder, M. F., and Samimy, M., "The Evolution of a Jet with Vortex-Generating Tabs: Real-Time Visualization and Quantitative Measurements," *Journal of Fluid Mechanics*, Vol. 311, 1996, pp. 73–118.

[9] Foss, J. K., and Zaman, K. B. M. Q., "Large- and Small-Scale Vortical Motions in a Shear Layer Perturbed by Tabs," *Journal of Fluid Mechanics*, Vol. 382, 1999, pp. 307–329.

[10] Pratte, B. D., and Keffer, J. F., "The Swirling Turbulent Jet," *Journal of Basic Engineering*, Vol. 94, Dec. 1972, pp. 739–747.

[11] Panda, J., and McLaughlin, D. K., "Experiments on the Instabilities of a Swirling Jet," *Physics of Fluids*, Vol. 6, No. 1, 1994, pp. 263–276.

[12] Liang, H., and Maxworthy, T., "An Experimental Investigation of Swirling Jets," *Journal of Fluid Mechanics*, Vol. 525, 2005, pp. 115–159.

[13] Kibens, V., and Wlezien, R. W., "Active Control of Jets from Indeterminate-Origin Nozzles," AIAA Paper 1985-542, March 1985.

[14] Wlezien, R. W., and Kibens, V., "Passive Control of Jets with Indeterminate Origins," *AIAA Journal*, Vol. 24, No. 8, 1986, pp. 1263–1270.

[15] Longmire, E. K., Eaton, J. K., and Elkins, C. J., "Control of Jet Structure by Crown-Shaped Nozzles," *AIAA Journal*, Vol. 30, No. 2, 1992, pp. 505–512.

[16] Longmire, E. K., and Duong, L. H., "Bifurcating Jets Generated with Stepped and Sawtooth Nozzles," *Physics of Fluids*, Vol. 8, No. 4, 1996, pp. 978–992.

[17] Webster, D. R., and Longmire, E. K., "Vortex Dynamics in Jets from Inclined Nozzles," *Physics of Fluids*, Vol. 9, No. 3, 1997, pp. 655–666.

[18] Lim, T. T., "On the Breakdown of Vortex Rings from Inclined Nozzles," *Physics of Fluids*, Vol. 10, No. 7, 1998, pp. 1666–1671.

[19] New, T. H., Lim, K. M. K., and Tsai, H. M., "Vortical Structures in a Laminar V-Notched Indeterminate-Origin Jet," *Physics of Fluids*, Vol. 17, No. 5, 2005, p. 054108.

[20] Gutmark, E., and Ho, C.-M., "Visualization of a Forced Elliptic Jet," *AIAA Journal*, Vol. 24, No. 4, 1986, pp. 684–685.

[21] Mehta, R. D., and Bradshaw, P., "Design Rules for Small Low Speed Wind Tunnels," *The Aeronautical Journal*, Vol. 73, Nov. 1979, pp. 443–449.

[22] Liepmann, D., and Gharib, M., "The Role of Streamwise Vorticity in the Near-Field Entrainment of Round Jets," *Journal of Fluid Mechanics*, Vol. 245, 1992, pp. 643–668.

[23] Hussain, F., and Zaman, K., "The Preferred Mode of the Axisymmetric Jet," *Journal of Fluid Mechanics*, Vol. 110, 1981, pp. 39–71.

[24] Jorgensen, F. E., *How to Measure Turbulence with Hot-Wire Anemometers—A Practical Guide*, Dantec Dynamics, DK-2740 Skovlunde, 2002, pub. 9040U6151.

[25] Ho, C.-M., and Gutmark, E., "Vortex Induction and Mass Entrainment in a Small-Aspect-Ratio Elliptic Jet," *Journal of Fluid Mechanics*, Vol. 179, 1987, pp. 383–405.

N. Clemens
Associate Editor